17.0 CHARACTERIZATION OF MICROSTRUCTURE EVOLUTION IN NICKEL-TITANIUM-HAFNIUM INTERMETALLICS

Sean Mills (Mines)
Faculty: Aaron Stebner and Mike Kaufman (Mines)
Industrial Mentors: Chris Dellacorte and Ron Noebe (NASA GRC)

This project initiated in Fall 2015 and is supported by CANFSA. The research performed during this project will serve as the basis for a Ph.D. thesis program for Sean Mills.

17.1 Project Overview and Industrial Relevance

The high hardness, high compressive elastic strength, and good corrosion resistance of ternary Ni-Ti-Hf alloys makes them optimum candidates for specialized bearing applications. In addition, aged Ni-Ti-Hf alloys exhibit superelastic hysteresis curves under compressive loading, which results in a nearly doubled toughness compared to conventional binary Ni-Ti **(Figure 17.1)**. Conventional superelastic Ni-Ti alloys are known to experience high hardness and high residual stresses upon rapid quenching, resulting in cracking and machining distortion, whereas secondary precipitates can over-coarsen if cooled slowly, thereby reducing the material hardness. This project is designed to elucidate the effects of hafnium additions on the structure and properties of Ni-Ti-Hf alloys, with an emphasis on bearing element performance. It will be shown that hafnium additions have a significant impact on the transformation kinetics, which results in reduced residual stresses while retaining the high strengths and hardnesses that are desirable for bearing applications.

This multimodal study will include rolling contact fatigue characterization, residual stress and hardness measurement and time/temperature/transformation studies of selected Ni-Ti-Hf alloys. Alloy optimization will be conducted by varying the nickel contents by 50.3 – 56.0 at. % and hafnium contents by 1.0 – 8.0 at. %. **Figure 17.2** outlines the optimized alloy design space of the project that shows varied nickel and hafnium contents. The sample compositions that have been tested in rolling contact fatigue are investigated via transmission electron microscopy (TEM) are highlighted in previous work [17.2] in addition to recent progress [17.3]. Likely outcomes to the study include further understanding of rolling contact fatigue performance, failure mechanisms, performance (hardness, strength, lifetime predictions) versus residual stresses, and a map of alloy design space to allow for optimization of Ni-Ti-Hf alloys for tribology applications.

17.2 Previous Work

17.2.1 Rolling Contact Fatigue

It is known that for nickel-rich compositions of Ni-Ti, and also ternary Ni-Ti-Hf compositions with low amounts of hafnium (~ 1 at. %), the Ni_4Ti_3 phase may be used for precipitation hardening without compromising the high hardness of the solid solution. In fact, the precipitates can also increase the hardness of the alloys. However, for Ni-Ti-Hf with greater amounts of Hf (8 at. % or more), Hf and Ni rich "H-phase" precipitates form instead of Ni_4Ti_3 and provide even greater strengthening. Therefore, it is hypothesized that H-phase precipitation can also provide superior hardness, resulting in superior wear performance in alloys under rolling contact fatigue (RCF) conditions. Testing of Ni-Ti-Hf samples using a three ball-on-rod set-up is imperative to ensuring this hardening behavior improves the component from an engineering standpoint.

A significant reduction in rolling contact fatigue performance has been observed in the $Ni_{54}Ti_{45}Hf_1$ alloy between 1.9 and 2.0 GPa. The brittle nature of spalling failures that are common in the specimens that failed at 2 GPa provide insight to the dominant failure mechanisms under Hertzian contact conditions [17.1]. Specifically, it was speculated that there must be a change in the uniaxial stress-strain behavior (for instance, the critical stress for martensite formation) in the range of 1.9-2.0 GPa that can be related to rolling contact fatigue performance. Thus, uniaxial compression testing on the same material as tested under RCF conditions was conducted to provide insight into the relationship between the critical contact stresses under fatigue conditions and the distinctive features on the stress-strain curves.

17.2.2 TEM Characterization

NiTiHf alloys with target compositions of $Ni_{56}Ti_{41}Hf_3$ and $Ni_{56}Ti_{36}Hf_8$ were made by induction-melting high-purity elemental constituents using a graphite crucible and casting into a copper mold. The ingots were homogenized in vacuum at 1050ºC for 72 h and then extruded at 900ºC at a 7:1 area reduction ratio. The extruded rods were sectioned into samples that were initially solution annealed at 1050ºC for 30 minutes and water quenched. Samples of each composition were then pre-aged at 300 ºC for 12 h and air cooled, and finally aged a second time at 500 ºC for 4 h and air-cooled. To isolate the effect of pre-aging on the functional properties of Ni-Ti-Hf alloys, other test samples were directly aged at 550ºC for 4 h after the solution-anneal treatment (without pre-aging at 300ºC for 12 h). Conventional and high-resolution transmission electron microscopy (HR-TEM), bright-field transmission electron microscopy and selected area electron diffraction microscopy of aged Ni-Ti-Hf samples was carried out using an FEI Talos TEM (FEG, 200 kV). The TEM foils were prepared by electropolishing in an electrolyte of 30% HNO_3 in methanol (by volume) at around −35ºC. To measure the average size and spacing of the H-phase and Ni_4Ti_3 precipitates in addition to observing precipitate morphology, several HRTEM taken from various regions were analyzed. A probe-corrected FEI Titan 1 was employed to take atomic resolution scanning transmission electron microscopy (HR-STEM) images of some of the microstructures. Digital Micrograph was utilized to extract diffraction information of the precipitates analyzed in the collected HRTEM and HR-STEM images.

Findings through these techniques indicate a significant change in microstructure and properties by adjustments in composition and secondary thermal processing. The effect of Hf addition shows a direct change in preference from one secondary precipitation type. In **Figure 17.3** Ni_4Ti_3 readily forms after solution anneal and water quench and in **Figure 17.4** H-phase slowly begins to nucleate and grow. At the 8 at. % Hf level, preference for fine H-phase precipitation resulted in higher toughness [17.2]. At the 3 at. % Hf level, preference for blocky Ni_4Ti_3 precipitation resulted in higher toughness [17.3]. The effect of secondary processing via multi-step heat treatments show a change in the precipitates formed in a given sample. A two-step heat treatment of solution heat treatment and water quenching, and then a secondary aging step at 550 ºC before air-cooling reveals only one precipitate type.

17.3 Recent Progress

17.3.1 Rolling Contact Fatigue and Uniaxial Compression

Continued work on $Ni_{56}Ti_{36}Hf_8$ and binary $Ni_{55}Ti_{45}$ alloys has been performed, which reveals a measureable increase in contact stress limit in the ternary alloy system. At 2.1 GPa, the rods begin to spall and fail along the raceway. When compared with the binary $Ni_{55}Ti_{45}$ system under the aforementioned heat treatment schedule, the uniaxial compression behavior of ternary $Ni_{56}Ti_{36}Hf_8$ alloy specimens are superior **(Figure 17.5)** achieving compressive yield stress of 3.4 GPa prior to buckling at 3.6 GPa. The published $Ni_{55}Ti_{45}$ compression behavior achieved a yield stress of 2.7 GPa before failing at 2.8 GPa [17.4]. The improvement in compression and fatigue performance is indicative that compositional adjustments (increasing hafnium levels slightly) and thermal processing via water quenching with additional higher temperature aging treatment play an important role in the longevity of the rolling contact fatigue specimens under compressive loads. During high cycle fatigue, however, the systematic failure and drop-off in performance at very similar stress levels leads to the conclusion that mechanisms other than compressive strength may affect fatigue performance. One possible explanation for the consistent failure could be that the tensile strength in these alloys is significantly lower than the compressive strength. Thus, brief changes in loading direction from compression to tension that regularly occur along the rolling contact fatigue wear track may be the cause of failure at approximately the tensile stress of the material.

17.3.2 TEM Characterization of 56 at. % Nickel Alloys

More recent findings on $Ni_{56}Ti_{41}Hf_3$ and $Ni_{56}Ti_{36}Hf_8$ alloys indicate the origins of secondary precipitation and their effects on material hardness. **Table 17.1** includes the reported Ni_4Ti_3 and H-phase precipitate sizes, inter-particle distances in each specimen considered, and specimen hardness. To study the effect of pre-aging treatment, the microstructure of $Ni_{56}Ti_{36}Hf_8$ and $Ni_{56}Ti_{41}Hf_3$ alloys after being solution annealed and pre-aged at 300ºC for 12 h was also investigated.

Three-step heat treatment was applied on $Ni_{56}Ti_{36}Hf_8$ alloy and the microstructure is shown in **Figure 17.6**. It is obvious from the BF micrograph and corresponding SAED pattern taken from the region indicated by the white circle in **Figure 17.6b** that the mottled-like morphology is much finer than the blocky structure for $Ni_{56}Ti_{41}Hf_3$ alloy. The

microstructure consists primarily of nano-sized dense H-phase and Ni_3Ti_2 precipitates. High resolution HAADF-STEM micrograph taken along the $[001]_{B2}$ zone and corresponding FFT pattern presented clearly shows the dense H-phase and Ni_3Ti_2 nano-precipitate formation within B2 channels. The average size of the ellipsoidal H-phase precipitates is 23 ± 5 nm (length) and 12 ± 3 nm (width) and the inter-particle distance is 7 ± 2 nm. The average size of the Ni_3Ti_2 precipitates is 25 ± 5 nm and can often be identified sandwiched between surrounding H-phase precipitates. The size of B2 channels is 8 ± 3 nm. The structure of the Ni_3Ti_2 precipitates was characterized as cubic structured Ni_3Ti_2. The basic structure of Ni_3Ti_2 is cubic with a lattice parameter of 8.74Å, ~ 3x the lattice parameter of the B2 austenite and, due to the cube-cube orientation relationship between the matrix and the Ni_3Ti_2 precipitates, the coherency is likely to strengthen the material similar to Ni_4Ti_3 by resisting particle shearing and restricting dislocation movement in a highly constrained matrix [17.5]. However, the exact structure and contribution to structure properties was not reported. Recent DFT analysis in collaboration with Yu Hong and Mohsen Asle-Zaeem at Mines allowed us to determine a stable cubic Ni_3Ti_2 BCC type structure **(Figure 17.7)** when compared with three different cubic type structures. The energy minimization curve **(Figure 17.7d)** shows that the BCC structure **(Figure 17.7c)** is the most stable compared to the SC **(Figure 17.7a)** and FCC **(Figure 17.7b)**. The corresponding lattice parameter of this BCC-type supercell is 8.74Å. The locations of Ni and Ti atoms within the super-cell showed that Ni atoms lie primarily on the edge positions while both Ni and Ti atoms lie in center positions. The unit cell structure and atomic positions were confirmed via atomic resolution STEM micrograph of a single Ni_3Ti_2 precipitate that shows edge positions with higher z-contrast (Ni) and center positions with lower z-contrast (Ni+Ti).

17.4 Plans for Next Reporting Period

- Continued work on rolling contact fatigue tests of optimized $Ni_{56}Ti_{36}Hf_8$ alloy.
- Continued microstructure characterization of 50-56 at. % Ni and 3-8 at. % Hf compositions for various heat treatments.
- Uniaxial compression testing of $Ni_{56}Ti_{41}Hf_3$ and $Ni_{56}Ti_{36}Hf_8$ alloys.
- Dent-damage tolerance testing of $Ni_{54}Ti_{45}Hf_1$ alloy.

17.5 References

[17.1] C. Dellacorte, M.K. Stanford, T.R. Jett. “Rolling contact fatigue of superelastic intermetallic materials (SIM) for use as resilient corrosion resistant bearings”, Tribology Letters, 2015, 57(3):1-10

[17.2] B.C. Hornbuckle, R.D. Noebe, G.B. Thompson. “Influence of Hf solute additions on the precipitation and hardenability in Ni-rich NiTi alloys”, Journal of Alloys and Compounds, 2015, 640:449-454

[17.3] K. Otsuka and X. Ren. “Physical metallurgy of Ti-Ni based shape memory alloys”, Progress in Materials Science, 2005, 50(5):511-678

[17.4] O. Benafan, A. Garg, R.D. Noebe, H.D. Skorpenske, K. An, N. Schell. “Deformation characteristics of the intermetallic alloy 60NiTi”, Intermetallics, 2017, 82:40-52

[17.5] M. Karlík, P. Haušild, M. Klementová, P. Novák, P. Beran, L. Perrière, J. Kopeček. “TEM phase analysis of NiTi shape memory alloy prepared by self-propagating high-temperature synthesis”, Advances in Materials and Processing Technologies, 2017, 3(1):58-69

[17.6] L. Casalena, A. N. Bucsek,D. C. Pagan, G. M. Hommer, G. S. Bigelow, M. Obstalecki, ... A. P. Stebner. “Structure-Property Relationships of a High Strength Superelastic NiTi–1Hf Alloy”. Advanced Engineering Materials, 2018, 20(9), 1800046.

17.6 Figures and Tables

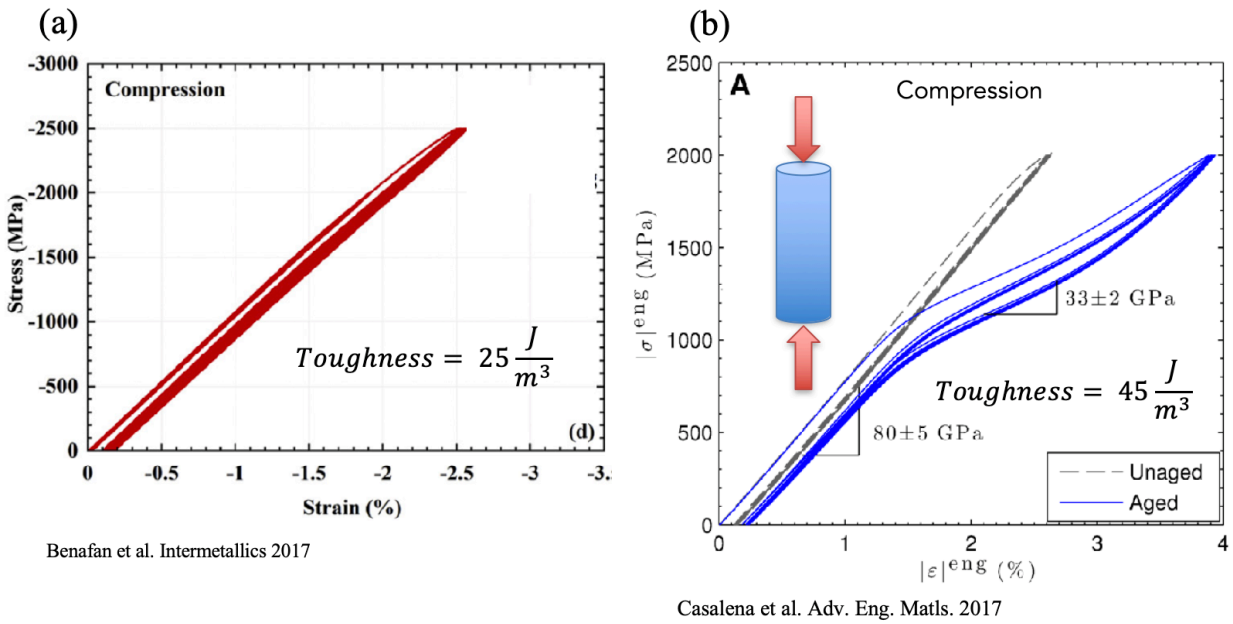

Figure 17.1: (a) 5-cycle compressive response of intermetallic $Ni_{55}Ti_{45}$ shows no super-elasticity [17.4]. (b) 5-cycle compressive response of $Ni_{54}Ti_{45}Hf_1$ shows super-elasticity with little to no hysteresis [17.6]. As a result, nearly doubled toughness in the ternary alloy compared to the binary alloy.

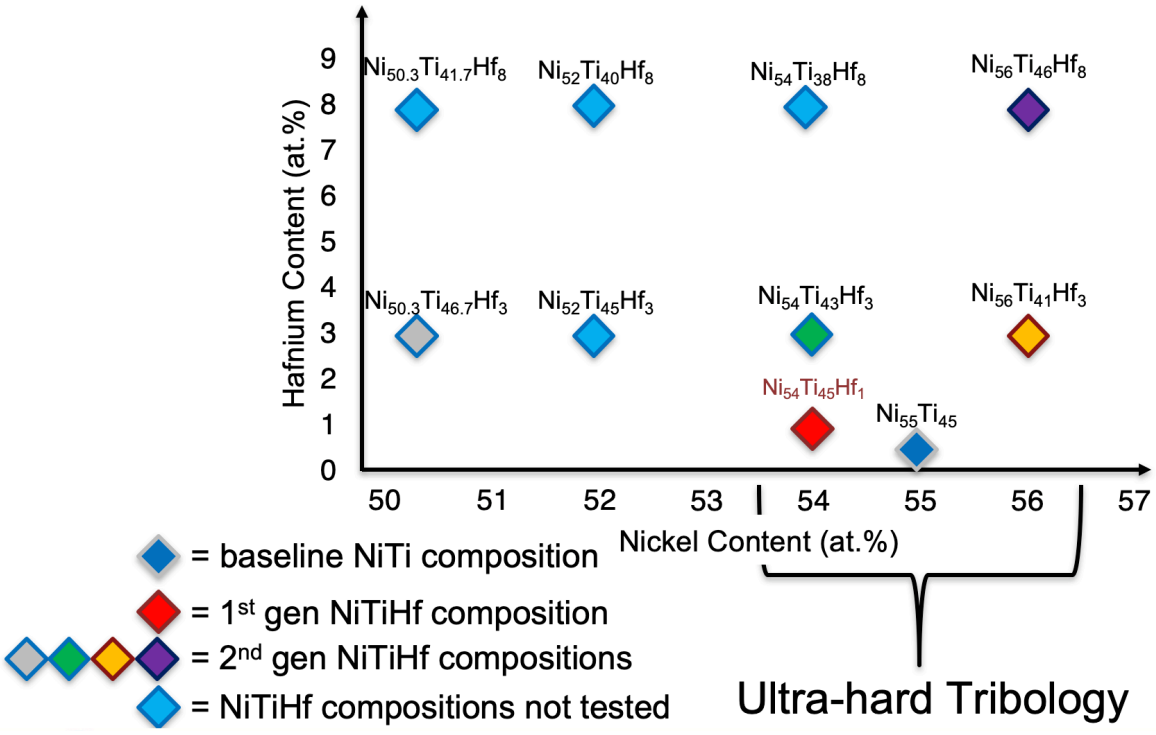

Figure 17.2: Target design space of NiTiHf alloys. Samples of interest to the project vary in nickel and hafnium content. Their applicability as shape memory alloys (SMAs), superelastic alloys, and bearing alloys are listed.

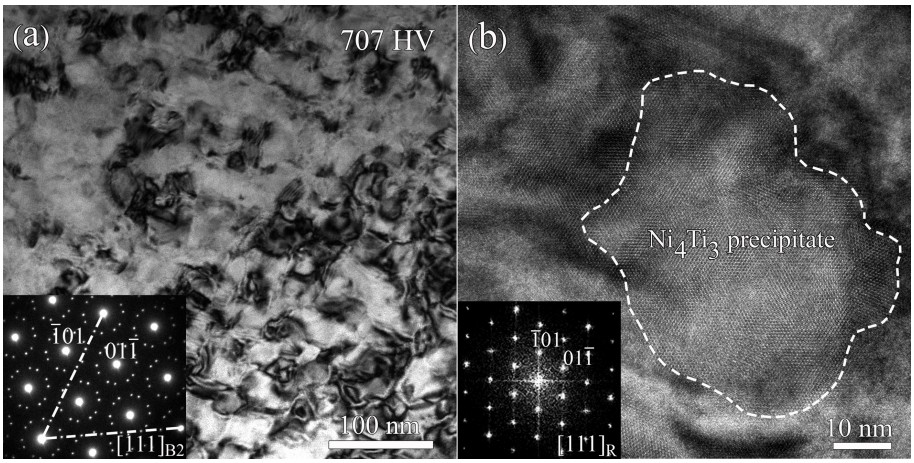

Figure 17.3: (a) Conventional BF-TEM micrograph of $Ni_{56}Ti_{41}Hf_3$ after solution annealing at 1050 °C for 0.5 h. Corresponding SAED pattern in the bottom left inset taken along $[111]_{B2}$ zone axis showing the super reflections originated from two variants of Ni_4Ti_3 precipitates. (b) HRTEM micrograph taken along $([111]_R // [111]_{B2})$ showing a monolithic Ni_4Ti_3 precipitate within B2 matrix.

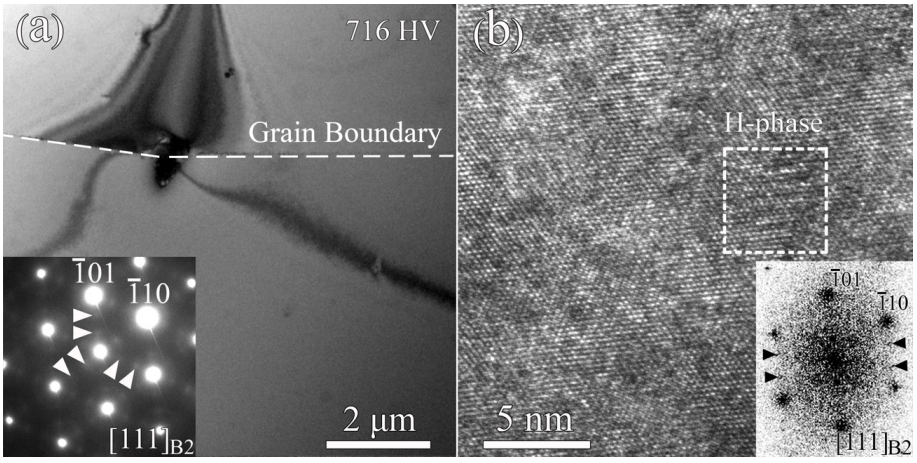

Figure 17.4: (a) BF-TEM micrograph of $Ni_{56}Ti_{36}Hf_8$ after solution annealing at 1050 °C for 0.5 h. Corresponding SAED pattern in the bottom left inset are taken along $[111]_{B2}$ showing the weak super reflections originated from 3 different variants of H-phase precipitates along 1/3<011> (indicated by arrowheads). (b) HRTEM micrograph taken along $[111]_{B2}$ showing a small H-phase precipitate. The super reflections originated from the H-phase precipitate are indicated by arrowheads in the FFT pattern.

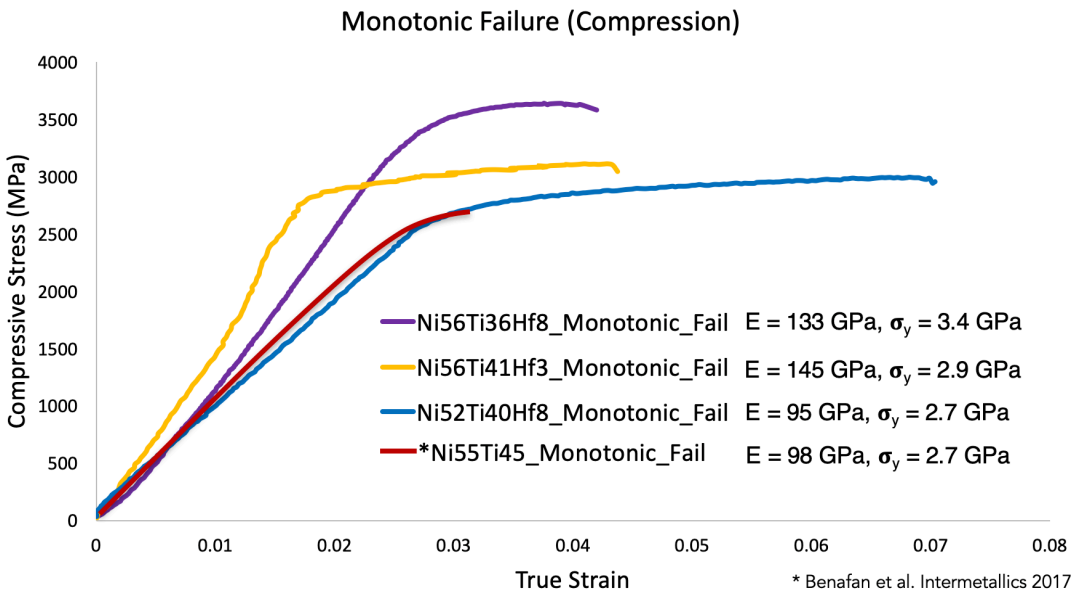

Figure 17.4: Monotonic compression response for $Ni_{56}Ti_{36}Hf_8$ alloy after 3-step heat treatment (purple), $Ni_{56}Ti_{41}Hf_3$ alloy after 3-step heat treatment (yellow), $Ni_{52}Ti_{40}Hf_8$ alloy after 3-step heat treatment (blue), compared with published compressive response of $Ni_{55}Ti_{45}$ [17.4].

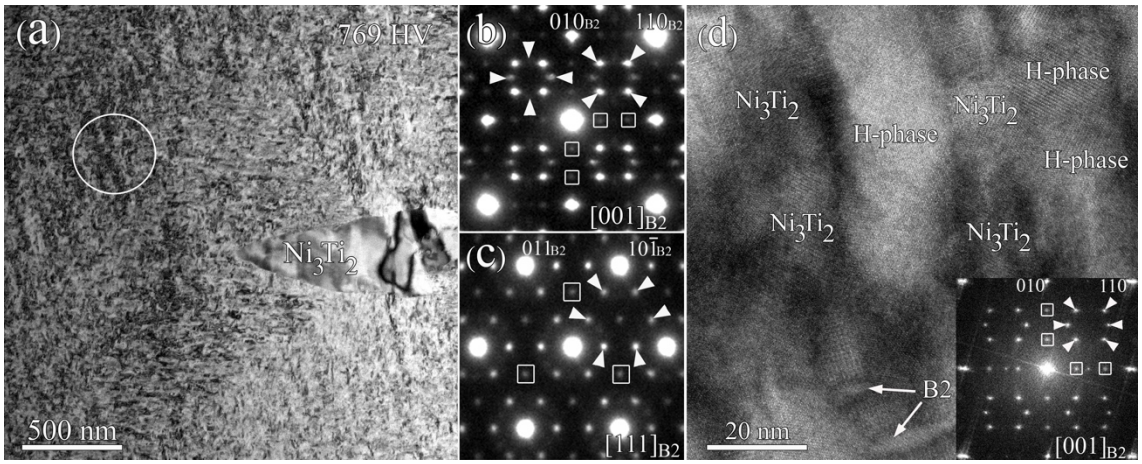

Figure 17.5: (a) BF-TEM micrograph of $Ni_{56}Ti_{36}Hf_8$ alloy after being solution annealed, pre-aged and aged at 550ºC for 4 h showing mottled-like microstructure. Heterogeneous Ni_3Ti_2 islands were also detected in this sample. (b) SAED pattern along $[001]_{B2}$ zone taken from the region indicated by white circle in (a) shows the existence of H-phase (white arrows) and Ni_3Ti_2 (white squares). (c) SAED pattern taken along zone ($[111]_{B2}$) also shows H-phase (white arrows) and Ni_3Ti_2 (white squares) formation. (d) HR-STEM micrograph taken along $[001]_{B2}$ zone axis and corresponding FFT (inset) reveals dense nano-precipitation of H-phase (white arrows) and Ni_3Ti_2 (white squares) within narrow B2 matrix. The locations of each secondary phase and the narrow B2 channels are labeled accordingly.

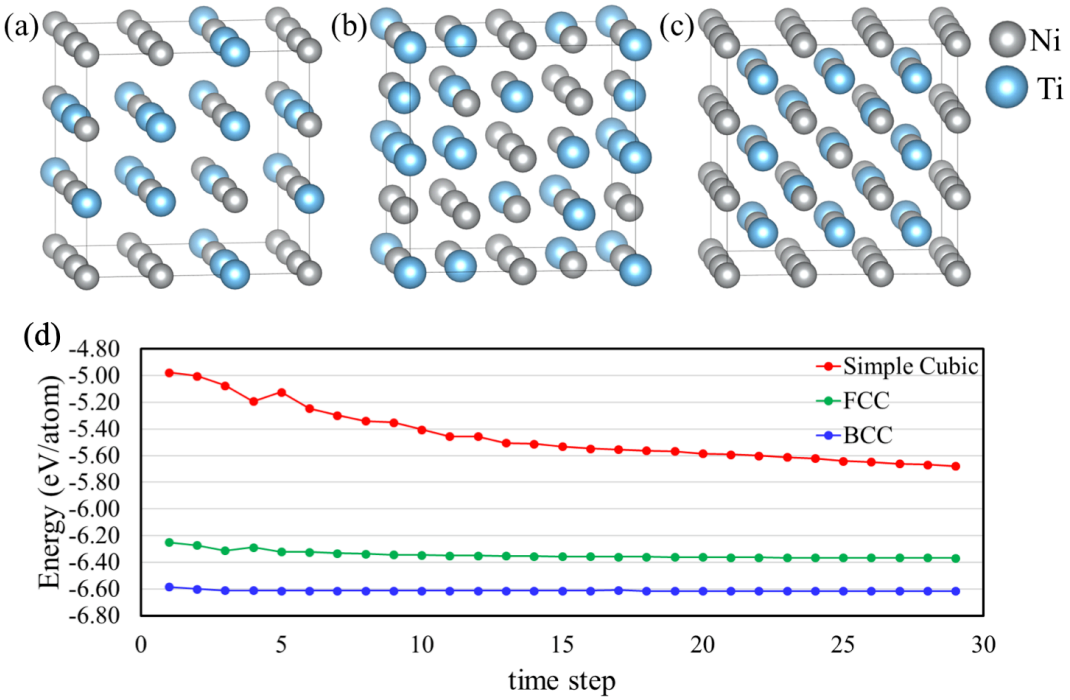

Figure 17.7: Ab initio density functional theory (DFT) calculations to analyze the crystal structure of the Ni_3Ti_2 precipitation. Figure 1. Cubic structures of Ni_3Ti_2 based on different lattices: (a) Simple cubic, (b) face-centered cubic, and (c) body-centered cubic (d) Energy minimization curve of the 3 cubic structures.

Table 17.1: Ni_4Ti_3 and H-phase precipitate size / nearest neighbor distances with respect to hardness

Composition / HT	Ni_4Ti_3 Length (nm)	Ni_4Ti_3 Width (nm)	Ni_4Ti_3 distance (nm)	H-Phase Length (nm)	H-Phase Width (nm)	H-Phase distance (nm)	Hardness (HV)
$Ni_{56}Ti_{41}Hf_3$ / WQ	63 ± 16	63 ± 16	42 ± 13	**	**	**	707 ± 9
$Ni_{56}Ti_{41}Hf_3$ / WQ + 550(4 h)	113 ± 32	87 ± 19	92 ± 24	**	**	**	682 ± 10
$Ni_{56}Ti_{41}Hf_3$ / WQ + 300(12 h)	65 ± 21	65 ± 21	51 ± 19	**	**	**	752 ± 7
$Ni_{56}Ti_{41}Hf_3$ / WQ + 300(12 h) + 550(4 h)	138 ± 41	94 ± 23	105 ± 33	28 ± 4	13 ± 2	104 ± 13	710 ± 2
$Ni_{56}Ti_{36}Hf_8$ / WQ	**	**	**	2 - 5	2 - 5	N/A	716 ± 4
$Ni_{56}Ti_{36}Hf_8$ / WQ + 550(4 h)	**	**	**	21 ± 6	8 ± 2	17 ± 6	700 ± 7
$Ni_{56}Ti_{36}Hf_8$ / WQ + 300(12 h)	**	**	**	2 - 5	2 - 5	N/A	705 ± 8
$Ni_{56}Ti_{36}Hf_8$ / WQ + 300(12 h) + 550(4 h)	**	**	**	23 ± 5	12 ± 3	7 ± 2	769 ± 7

**Phase does not exist